



**HAL**  
open science

## Damage detection with ultrasonic guided waves using machine learning and aggregated baselines

Vivek Nerlikar, Olivier Mesnil, Roberto Miorelli, Oscar D'almeida

► **To cite this version:**

Vivek Nerlikar, Olivier Mesnil, Roberto Miorelli, Oscar D'almeida. Damage detection with ultrasonic guided waves using machine learning and aggregated baselines. *Structural Health Monitoring*, 2023, 23 (1), pp.443-462. 10.1177/14759217231169719 . hal-04547805

**HAL Id: hal-04547805**

**<https://hal.science/hal-04547805>**

Submitted on 18 Apr 2024

**HAL** is a multi-disciplinary open access archive for the deposit and dissemination of scientific research documents, whether they are published or not. The documents may come from teaching and research institutions in France or abroad, or from public or private research centers.

L'archive ouverte pluridisciplinaire **HAL**, est destinée au dépôt et à la diffusion de documents scientifiques de niveau recherche, publiés ou non, émanant des établissements d'enseignement et de recherche français ou étrangers, des laboratoires publics ou privés.

# Damage detection with ultrasonic guided waves using machine learning and aggregated baselines

Vivek Nerlikar<sup>1</sup> , Olivier Mesnil<sup>1</sup>, Roberto Miorelli<sup>1</sup>   
and Oscar D'Almeida<sup>2</sup>

## Abstract

In guided wave (GW)-based structural health monitoring (SHM), ultrasonic elastic waves are used to detect damages in structures by comparing the acquired signals with those acquired before defect formation. Making the SHM system automatic, especially for similar structures, such as turbine blades, is rather challenging. The high sensitivity of GWs to environmental and operational conditions, the variabilities due to sensor positioning, sensor coupling, and material variability in composites limit the baseline application. This work presents a machine learning (ML)-based damage detection method using aggregated baselines independent of their damaged states to enhance the generalization capability of ML algorithms by considering similar structures' variabilities. The methodology relies on feature extraction from raw GW signals and training classification algorithms (e.g., kernel machines, ensemble methods, and neural networks). Two experimental data sets on composite panels are used. The first experimental data set of 45 composite panels is used to validate the approach by considering the aforementioned inter-specimen variabilities. Half of the 45 panels provide pristine data, and the rest provide damaged data so that the same sample is present in the training or test set but never in both. High classification performance is obtained, demonstrating that the classifier has successfully learned to recognize defect signatures despite the influence of the variabilities linked to the multiple instrumented specimens. The second experimental data set of 1 composite panel with temperature variation is used. Good classification performance is obtained without using baseline correction methods.

## Keywords

Ultrasonic guided wave SHM, kernel machines, ensemble methods, deep learning, temperature variation, composite materials

## Introduction

Structural health monitoring (SHM) is implementation of damage detection strategies for structures by means of permanently embedded sensors acquiring information seamlessly.<sup>1</sup> This information is later processed to diagnose the state of the structure. Different types of SHM systems have already been proposed; among them are vibration-based and guided wave-based SHM (GW-SHM).<sup>2</sup> The latter uses ultrasonic sound waves for inspection, which can travel long distances and are highly sensitive to defects. The potential areas of GW application are pipeline inspection (oil and gas industries), bridges, and aircraft structures.

In GW-SHM, a pair of piezoelectric transducers are used; one acts as an emitter and the other as a receiver placed away from the emitter. The emitted GWs interact with the defect, which causes changes to the

waveform, such as, change in amplitude and/or change in phase.<sup>3</sup> This change in the signals is then identified by subtracting the acquired signal with a reference signal measured on undamaged state. The resulting residual signal is the indication of the presence of a defect; this approach is called *baseline subtraction*.<sup>3</sup> However, GWs are not just sensitive to defects but also to environmental and operational conditions, material properties, and transducer coupling; for example, increasing temperature reduces the stiffness of the material that in

---

<sup>1</sup>Université Paris-Saclay, CEA-List, Palaiseau, France

<sup>2</sup>SAFRAN Tech, Chateaufort, Magny-Les-Hameaux, France

### Corresponding author:

Vivek Nerlikar, Université Paris-Saclay, CEA, List, 91120, Palaiseau, Gif-Sur-Yvette 91191, France.

Email: vivek.nerlikar@cea.fr

turn changes the wave speed. Hence, the variation in the temperature of the current state must be limited to ensure the reliability of baseline subtraction method. Along with temperature, other influences on GW propagation are listed in the study by Gorgin et al.<sup>4</sup> With the influence of aforementioned factors, baseline subtraction becomes ineffective.

The literature offers numerous baseline correction methods that mainly focus on temperature compensation. Optimal baseline selection,<sup>5</sup> is one in which the residual signal amplitude is minimized until an optimal baseline is selected from the pool of acquired baselines. In baseline signal stretch technique proposed by Croxford et al.,<sup>6</sup> the current signal is stretched until it matches with the baseline. A big pool of baselines is required for optimal baseline selection method which is not practical, and baseline signal stretch alters the frequency content of the signal which is not effective for higher temperatures.<sup>4</sup> Other proposed methods are, combination of the above two methods<sup>7</sup> and dynamic time warping. An optimal mapping between two time series with changing amplitude or speed is determined in dynamic time warping.<sup>8</sup> Other temperature compensation methods requiring a baseline/a set of baselines include those given under references.<sup>9–12</sup> The efficiency of these methods degrades when the temperature of the test specimen is beyond the range considered for acquiring baselines.<sup>13</sup> Improved baseline signal stretch methods listed in the review paper by Gorgin et al.<sup>4</sup> can be effective for a temperature difference of 18°C. Kulakovskiy<sup>14</sup> showed in his thesis that, dynamic time warping is effective for a temperature difference of up to 25°C. The aforementioned methods, however, employ alignment of the baseline signals, and their main focus is temperature compensation alone, but other environmental conditions, sensor variability, and so on also affect GW signals.<sup>4</sup>

Baseline-free approaches have been proposed to overcome the baseline dependency. Time reversibility of lamb waves,<sup>15</sup> transfer impedance of transducers,<sup>16</sup> cross-correlation analysis proposed by Alem et al.<sup>17</sup> are some of the baseline-free methods listed in the review paper by Gorgin et al.<sup>4</sup> The baseline-free techniques utilize mainly the signal energy, and because environmental and operational conditions also modify the amplitude of the signal, these techniques become less effective.<sup>4</sup> In recent times, the use of machine learning (ML) and deep learning is increasing in defect detection and localization in GW-SHM. Miorelli et al.<sup>18,19</sup> employed post-processed GW-imaging to train kernel machines, but ultrasound- and GW-based images are constructed using residual states obtained from baseline subtraction. Schnur et al.<sup>20</sup> worked on the detection of temperature-affected signals using standard classifiers and features. However, the temperature

effect was compensated through optimal baseline selection and baseline signal stretch. Rautela et al.<sup>21</sup> showed good classification performance on a composite panel using a One-Dimensional Convolutional Neural Network (NN). The aforementioned works depend on baseline correction and do not present the study on the robustness of the developed methodology concerning similar structures or when baselines are unavailable.

ML-based damage detection in GW-SHM results in a configuration-specific monitoring scheme, which means that the structure on which a ML model is trained cannot be used for the diagnosis of other similar structures, let alone other arbitrary structures. To achieve a real-time automatic monitoring GW-SHM system for similar structures, the generalization capability of ML models needs to be enhanced. It can be accomplished by taking into account the inter-specimen variability across multiple similar instrumented structures. These variabilities include material properties, sensor position, sensor coupling, defect location, shape and size, and environmental and operational conditions. The main goal of this work is to develop a robust damage detection scheme for similar structures.

To conduct the research, we considered two distinct data sets. The first one (in-house measurement data set) contains inter-specimen variabilities as a result of measurement data coming from 45 carbon fiber reinforced polymer (CFRP) panels and has minor temperature variation (i.e.,  $20 \pm 2^\circ\text{C}$ ). Therefore, the Open guided wave (OpenGW) data set<sup>22</sup> is considered, which contains more significant temperature variation (i.e.,  $[20^\circ\text{C}, 60^\circ\text{C}]$ ). The methodology consists of baseline aggregation, AutoRegression (AR) for extracting features from the signals under the influence of variabilities without correcting the baselines and classification. The supervised ML classifiers are used to classify the two states. Furthermore, variability inclusion through multiple structures aid in improving the generalization capability of ML models. The most recent works on the OpenGW data set include applying baseline correction methods to compensate for temperature effect.<sup>20</sup> And Abbassi et al.<sup>23</sup> perform damage classification without relying on baseline correction but consider temperature groups with shorter ranges (i.e.,  $10^\circ\text{C}$  temperature difference). We conducted the study on the OpenGW data set by applying AR modeling and baseline aggregation methodology to avoid using baseline correction methods and considering temperature groups with a more comprehensive temperature range (i.e., up to  $40^\circ\text{C}$ ).

Experimental setup and data description is first presented in methodology section. Then data annotation process is explained, in which significant defect information-carrying signals in damaged panels are separated from those carrying less significant

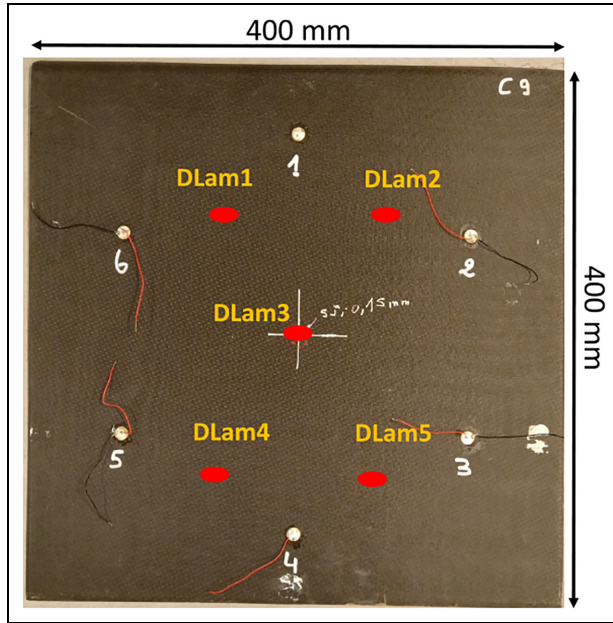


**Figure 1.** A sample CFRP panel of size 400mm  $\times$  400 mm instrumented with six PZT sensors. The elliptical marker (①) shows five delamination locations (i.e., DLam1, DLam2, DLam3, DLam4, and DLam5). Note that the delamination is present at either one of the five locations given a single panel. CFRP: carbon fiber reinforced polymer; PZT: piezoelectric transducer.

information. The following section explains baseline aggregation procedure. Then feature extraction process, experimental validation, discussion, and conclusion are presented in the subsequent sections.

## Methodology

### Data description

The experimental set up consists of 45 CFRP panels. Each of the panels is instrumented with 6 PZT transducers distributed over a 150-mm radius circle, one sample instrumented panel is shown in Figure 1. In this experiment, delamination type defects are induced by means of impacting each panel with a 16-mm radius steel head and no second impact was allowed. The 45 panels are impacted at different locations within the circle defined by the sensor network.

GWs were generated by using a two-cycles tone burst waveform and four excitation frequencies namely, 40, 60, 80, and 100 kHz are used for measurement. The size of the delamination to be detected drives frequency selection. But for higher frequencies, multiple modes exist, and there is an overlap of modes, which does not allow for the extraction of proper time of flight (ToF) information. Therefore the four

frequencies' selection is a trade-off between damage detectability and mode overlap. Signal acquisition was carried out by exciting the transducers in round robin fashion, thereby acquiring 15 unique signals per panel at a sampling frequency of 5 MHz.

Signal acquisition was first completed on 45 pristine panels. Later, the impact-caused delamination of varying sizes and at either one of the five different locations as shown in Figure 1 were created on all 45 panels, and damaged state signals were acquired. Three sample signals of shortened length are shown in Figure 2 to illustrate the complexity in the signals caused by intra- and inter-specimen variabilities. The pristine signals do not overlap in both the cases (see Figure 2(a)) despite the absence of flaw; this implies the presence of some factors influencing the GWs. Similarly, in damaged state signals, these variations are present along with variations due to defects (see Figure 2(b)). These changes can be attributed to Inter-Specimen and Intra-Specimen Variabilities. The prior contains variabilities of multiple specimens, such as material properties,<sup>24</sup> sensor positioning and coupling, defect size, and location, whereas the latter contains sensor coupling and material properties. The influence of these variabilities on the considered data set is listed in Table 1. The illustration of sample signals suggests that the effect of these variabilities is dominant and may mask the changes due to defect; this poses a challenge in the defect identification task.

### Damage path identification

In a pitch-catch measurement method and for a specific defect location, the amount of defect-related information contained by all the paths differs. When the defect is at the center, as shown in Figure 1, not all the paths carry defect information provided windowing based on the arrival of A0 mode. In other words, the adjacent paths (1–2, 2–3, 3–4, 4–5, and 5–6) may carry minimal defect information. Hence, the paths containing significant defect information need to be separated from those not containing. This procedure works as a preprocessing stage in a ML-based classification pipeline. Furthermore, this step is essential to appropriately annotate the data required for supervised ML algorithms. The following steps describe the procedure involved in the signal separation process.

### Signal treatment and data annotation

**Filtering.** In the path identification process pristine and defect signals are compared. Therefore to better learn the effect of a defect, both signals are filtered with a fifth order Butterworth filter allowing

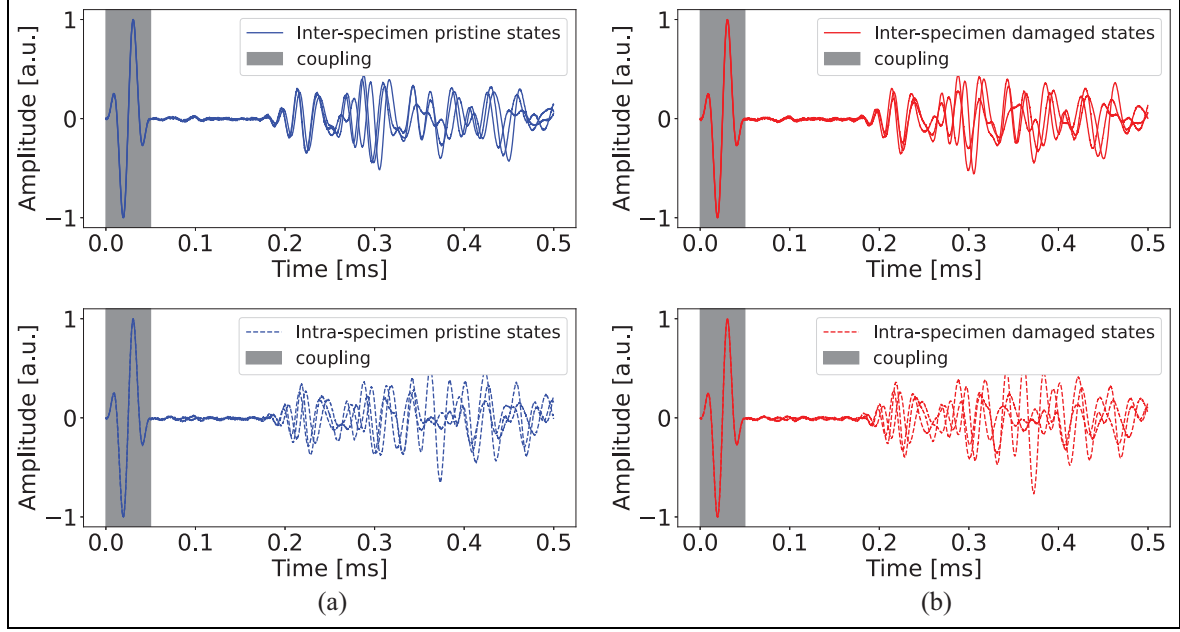


**Figure 2.** (a) Inter-specimen variabilities: normalized signals corresponding to path 1–4 of three instrumented pristine panels and intra-specimen variabilities: normalized signals corresponding to three paths (similar paths) of one pristine panel, that is, 1–4, 2–5, and 3–6; (b) effect of inter (top) and intra-specimen (bottom) variabilities in damaged case (considering similar paths as in pristine case).

frequencies between 20 kHz and  $2 \times F_c$ , where  $F_c$  is the center frequency of excitation.

**ToF-based windowing.** Signal windowing helps remove the reflections depending on the length of the window. The length of a window is decided based on the ToF. It is calculated based on the velocity of the GW-mode, and the path traveled. The velocity of GW-modes is determined from dispersion diagrams. In an anisotropic medium the GW-modes propagate with varying velocities as a function of propagation angle. But for the CFRP panel used in this study they exhibit minimal variation in the group velocities, which is shown in Figure 3(a). Therefore, an average of the velocities is computed (see Figure 3(b)) and used to estimate the ToF.

For the considered frequencies A0 mode is more sensitive to the defect sizes present in the dataset than S0 mode; therefore A0 mode is used for damage detection process. The ToF of A0 mode is computed by a simple velocity, distance, and time relationship which is given below,

$$\text{ToF}(f) = \frac{d}{C_g(f)} \quad (1)$$

where,  $d$  is the distance between a sensor pair (path) and  $C_g(f)$  is the average group velocity as a function of frequency. All the paths have been grouped into three

**Table 1.** List of intra-specimen and inter-specimen variabilities.

Variability	Intra-specimen variability	Inter-specimen variability
Measurement noise	Present	Present
Sensor positioning	Absent	Present
Sensor coupling	Present	Present
Defect size and shape	Present	Present
Material properties	Absent	Present

groups. The first group contains the adjacent paths (i.e., the peripheral paths), the second one contains paths (1–3, 1–5, 2–6, 2–4, 3–5, 4–6), and the third group consists of paths (1–4, 2–5, 3–6) (refer to Figure 1). The ToFs for each path are then calculated with the corresponding distance average group velocity. Similarly, the electromagnetic coupling is also windowed by calculating the time of the excitation pulse ( $t_{\text{coup}}$ ), that is,  $t_{\text{coup}} = N_{\text{cyc}}/F_c$ , where  $N_{\text{cyc}}$  is the number of cycles in the excitation pulse and  $F_c$  is the excitation frequency.

Since the CFRP panel used in the study exhibits negligible changes in the group velocities at different directions, a representative velocity is considered by taking an average of all the velocities. In the case of strong anisotropy, the representative velocity needs to be replaced by individual directional group velocities to extract the ToF information.

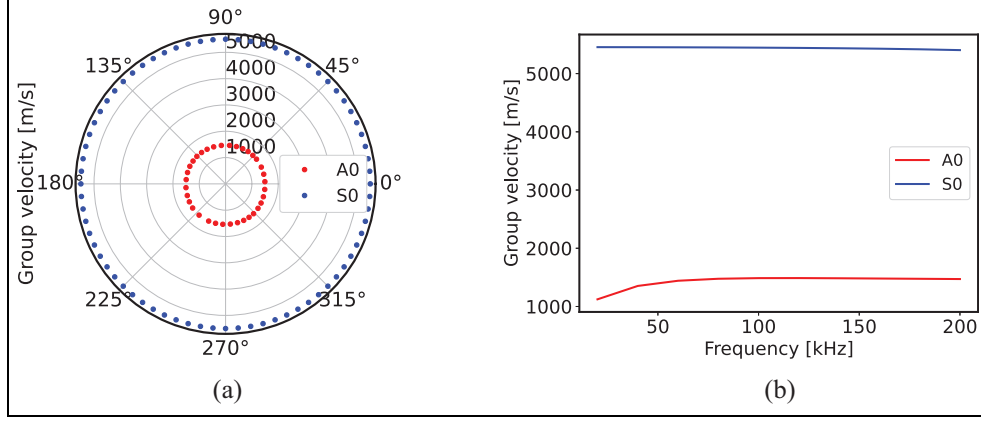


**Figure 3.** (a) Polar dispersion diagram containing A0 and S0 group velocities at different propagation angles and (b) the averaged group velocity diagram containing average A0 and S0 group velocity.

**Damage index.** To quantify significant defect carrying signals, root mean squared deviation (RMSD) as a damage index (DI) is employed. It accounts for the overall changes in a signal by comparing it with a defect-free signal. The mathematical expression of RMSD is shown in Equation (2),

$$\text{RMSD} = \sqrt{\frac{\sum_{i=1}^n (S_p(i) - S_d(i))^2}{\sum_{i=1}^n (S_p(i))^2}} \quad (2)$$

where,  $S_p$  and  $S_d$  are pristine and damaged signals respectively.  $(S_p - S_d)$  is the residual signal, and  $i$  corresponds to  $n$  time samples.

**Threshold selection.** For supervised ML algorithms, appropriate data annotation is a crucial step. Therefore, appropriate annotation of the signals is accomplished based on the DI obtained for each path in a damaged panel. Not all the paths might carry significant defect information for a specific delamination location in a panel. Referring to Figure 1, where the defect is at the center of the panel, considering the TOF corresponding to just the sensor paths (1–2, 2–3, 3–4, 4–5, 5–6), the GWs do not interact with the defect at all by the time they reach the receiver. Figure 4(b) shows calculated RMSD versus 15 unique paths for defect at the center. Higher DIs correspond to the direct paths, and for defects away from the sensor paths, DI decreases. Similar phenomena is observed for other two defect locations which is shown in Figure 4(a) and 4(c). A threshold is applied to facilitate the separation of higher DI from lower ones. The selection of this threshold is a tricky task and is arbitrary in a way. A higher threshold aiming at picking just very high DIs would lead to data scarcity, which is not desirable, as enough data is required to train ML

classifiers. Hence, as a trade-off, a threshold of 0.1 is selected to allow sufficient data in the defect category.

**Baseline aggregation.** In developing an automatic damage detection system for similar structures, the idea is to use a few damaged and a few pristine structures (aggregated baselines). Using aggregated baselines to train the models ensures the coverage of the variability and ensures monitoring of new similar structures even without the availability of baselines. Forty-five panels are divided into two groups to work on this idea. Pristine signals are considered from the group 1 and defect signals from group 2 (see Table 2). The latter group consists of damage-annotated signals resulting from the path identification process. This intermediary step ensures that the baseline signals of the damaged panels are not present in the data set (Figure 5).

A quantification of the pristine and damaged-state signals at the end of data annotation process is presented in Table 2. From here on pristine annotated signals are referred to group 1 signals only and defect annotated signals to group 2.

### Feature extraction

The effect of delamination on the GW signals is masked by the presence of inter- and intra-specimen variabilities. Therefore, instead of compensating the effect of the aforementioned variabilities, a feature extraction method is required to extract the defect signatures hidden under the influence of variabilities. Some of the feature extraction methods applied on GW signals include: principal component analysis for extracting features from post processed GW signals<sup>18</sup> and various feature extraction methods, such as



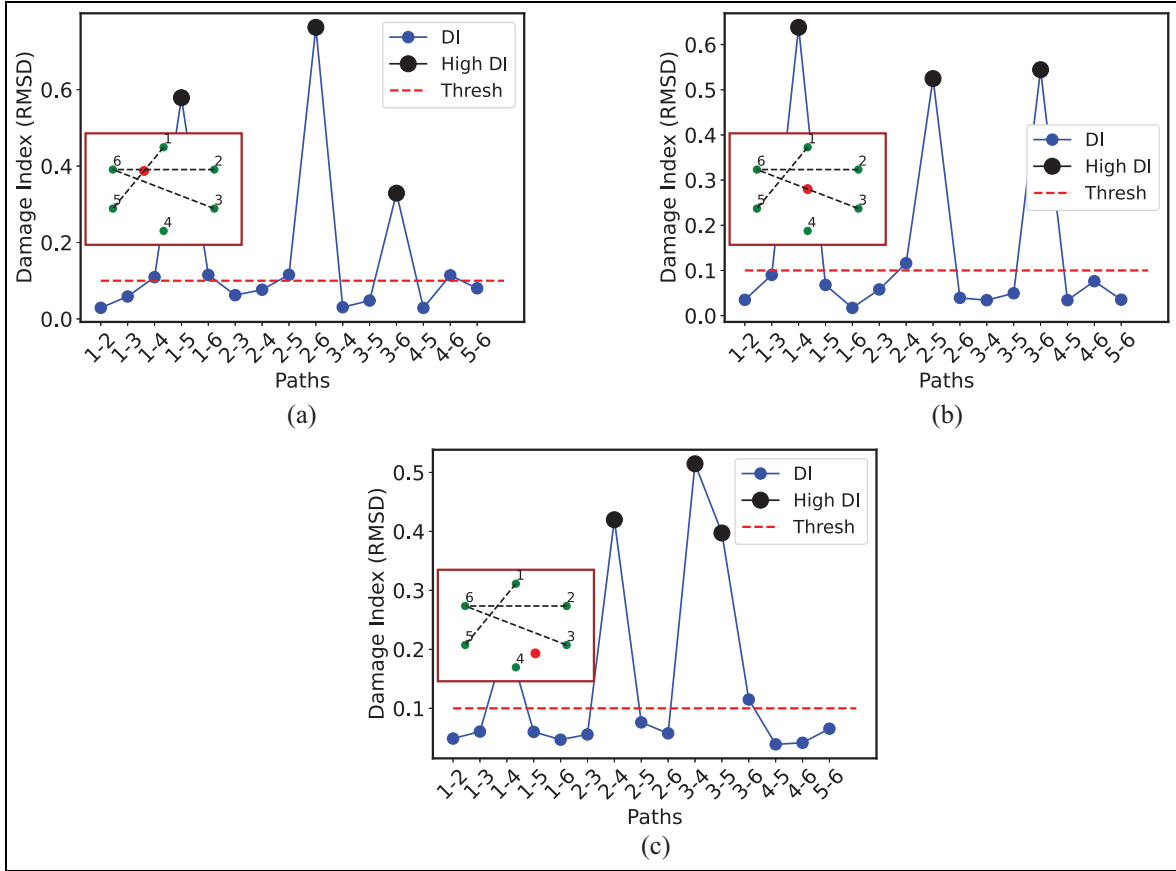


**Figure 4.** Defect configuration with delaminations at (a) (250, 135) mm, (b) (200, 200) mm, and (c) (150, 300) mm, and their corresponding damage index plots.

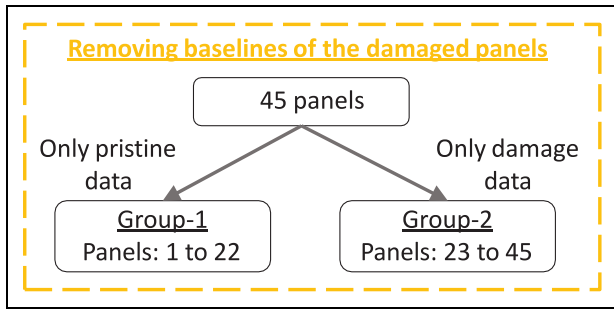


**Figure 5.** Schematic describing removing baselines of the damaged states. This step ensures that the pristine and damage acquisitions correspond to distinct panels.

principal components and best Fourier coefficients as presented in the study by Schnur et al.<sup>20</sup> The aforementioned feature extraction methods have been shown effective on baseline-corrected signals. But this work aims not to use classical baseline correction methods but instead apply a feature extraction method to extract features hidden under the influence of variabilities. Therefore, AR modeling is employed in this study

**Table 2.** Details of data set preparation.

Dataset	Group 1 (pristine)	Group 2 (defect)
Number of panels	22	23
Unique signals per panel	15	15
Frequencies	4	4
Total signals	1320	1380
<i>Result of path identification and signal annotation</i>		
Signals annotated as defect	0	693
<i>Final amount of pristine and defect signals from each group</i>		
Final total	1320	693

Number of defect signals after path identification and number of baseline aggregated signals.

to extract the hidden defect signatures from raw time domain signals.

AR is a linear combination of immediate preceding values in a sequence.<sup>25</sup> In other words, when a time

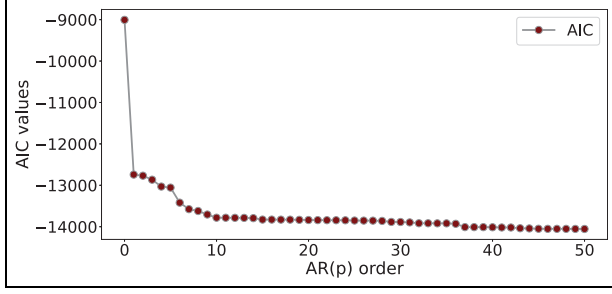


**Figure 6.** AR model order selection using AIC.  
AR: AutoRegression; AIC: Akaike Information Criterion.

series is stationary, then modeling the time series on past values yield the current value. A  $p^{\text{th}}$  order AR model can be represented mathematically as shown in Equation (3).

$$y(t) = \sum_{j=1}^p \Phi_j y(t-j) + \epsilon_t \quad (3)$$

where,  $y(t)$  is the current observation,  $y(t-j)$  is the lag,  $\Phi_j$  is the AR model parameter and  $E_t$  is the white noise term. Unknown model parameters  $\Phi_j$  can be estimated by employing algorithms such as, least square approach and Yule-Walker approach; furthermore, in SHM, these parameters can be used as damage-sensitive features.<sup>26</sup> Model parameters are determined by fitting an AR model on GW signals.

Selection of AR model order is a delicate task, because, higher model orders tend to show poor generalization and lower model orders may not capture the underlying dynamics of the system.<sup>27</sup> Therefore, model order  $p$  should be chosen in such a way that it

minimizes some model selection criteria. Akaike, Schwarz-Baysian, and Hannan-Quinn are the three common information criteria used to determine the order of an AR model.<sup>28</sup> All the criteria yielded similar trends in model selection, therefore only Akaike Information Criterion (AIC)-based model order selection plot is presented in Figure 6 and its statistic is defined below.

$$\text{AIC} = 2p - 2\log(\mathcal{L}_{LH}) \quad (4)$$

Where  $p$  is the number of model parameters estimated and  $\mathcal{L}$  is the maximum likelihood of the model with  $p$  model parameters. Figure 6 depicts the AIC values as a function of the AR model order. The trend of the plot suggests that, the AIC values start stagnating after model order 37. A model order of 40 is chosen to model GW-signals and in turn extract the features from them.

On each windowed raw signal AR model of order 40 is fitted, and the result is 40 encodings (AR model parameters) per signal; the final feature matrix of size  $[N \times 40]$  is formed, where  $N$  is the total number of signals (both pristine and defect). The parameter distribution is reordered as a function of decreasing difference between the means of pristine and defect feature distributions, which is shown in Figure 7. Along the  $X$ -axis are the 40 parameters, and variation in the model parameters is along the  $Y$ -axis. Each of the pristine and defect box plots consists of an equal number of pristine and defect features since the AR model is fit on balanced data set.

The first ten reordered pristine and defect feature distributions have less overlap than the rest, meaning that the AR model is sensitive to damage information in the presence of the variabilities. This discrimination

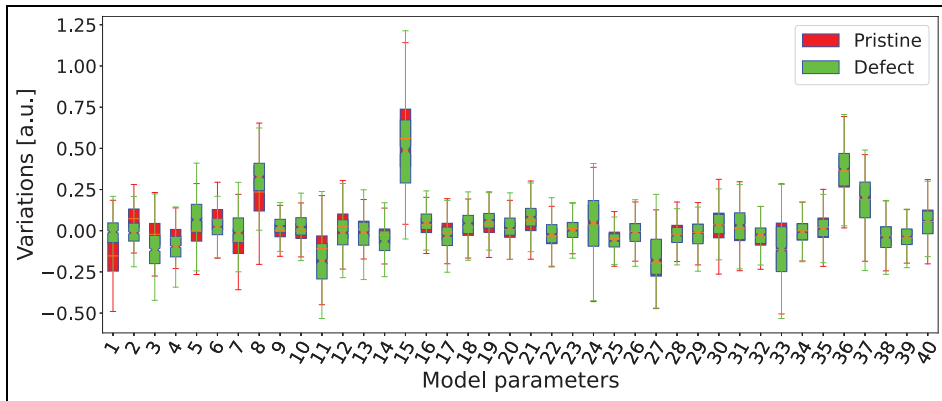


**Figure 7.** Box plot of reordered AR parameters in the decreasing order of the difference between the means of pristine and defect distributions.  
AR: AutoRegression.



between pristine and defect feature distributions may be exploited using ML algorithms.

### Background of classification algorithms

In SHM, ML algorithms have been used for damage detection and quantification tasks. Some of the established ML algorithms in SHM are listed as follows: Naive Bayes (NB) and kernel-based classifiers,<sup>18</sup> ensemble methods: random forest (RF) classifier<sup>29</sup> and extreme gradient boosting,<sup>30</sup> and convolutional NN.<sup>21</sup> Five different established classifiers from different families of algorithms are chosen to learn the AR encodings. The NB classifier, however, is used as a reference classifier to compare the performance with others. The description of the chosen classifiers is presented below.

**NB classifier.** NB classifier is based on the Bayes theorem. Consider a random vector  $(X, Y)$  consisting of feature vector  $X = (x_1, x_2, \dots, x_m)$  with cardinality  $m$  and class label  $Y$  with  $k$  labels. For  $k \in 1, 2, \dots, K$  classes, the prior probability can be given as,  $\pi_k$ . The likelihood of  $X$  given a class label has a probability density function,  $\Theta_{ok}(x)$ , where  $\Theta_k = (\Theta_{1k}, \dots, \Theta_{mk})$ .

According to the Bayes decision theory, a new observation  $X' = (x'_1, x'_2, \dots, x'_m)$  is classified into a class based on the conditional distribution. Moreover, the observations are assumed to be independent (conditioned on to a class) to simplify the estimation process in case of multiple features.<sup>31</sup> With conditional independence assumption, the decision rule assigning an observation to a class is given as,

$$\pi_k \prod_{o=1}^m \Theta_{ok}(x'_o) \geq \pi_r \prod_{o=1}^m \Theta_{or}(x'_o); \forall r = 1, \dots, K \quad (5)$$

**Support vector machines.** Support vector machines (SVM) algorithm constructs a hyperplane on the training data to separate two classes. Two parallel lines on both sides of a hyperplane exist, called the width/slab. SVM tries to maximize this width, and if this maximum width has no internal training samples, then the hyperplane is said to be best, and the samples lying on the margin are called support vectors.<sup>32</sup> For a linearly separable data, the best hyperplane can be represented by  $y_e(w \times x_e + b) \geq 0$ , where  $x_e$  and  $y_e$  are vectors along with their classes respectively and  $w$  is the unknown normal vector. When the data is not linearly separable, SVM allows for misclassification of some samples but classifies most of them correctly, and this is known as a soft margin.<sup>33</sup> The soft margin is formulated by adding slack variables  $\zeta l$  and a penalty parameter  $C$ . The soft margin formulation (minimization problem) is also known as the primal problem presented below.

$$\min_{w, b, \zeta} \frac{1}{2} w^T w + C \sum_{l=1} \zeta l \quad (6)$$

Dual problem of the soft margin is formulated for easier computations using Lagrange multiplier  $\alpha$ . The objective function of the dual problem is shown below.

$$L_{svm} = \sum_e \alpha_e - \frac{1}{2} \left( \sum_e \sum_g \alpha_e \alpha_g y_e y_g x_e \times x_g \right) \quad (7)$$

The optimization depends on the dot product of pair of training samples  $(x_e \cdot x_g)$ . Similarly, primal and dual problems can be formulated for nonlinear SVM by using kernel functions. Details on nonlinear SVM can be found in the studies by Boser et al.<sup>32</sup> and Kecman.<sup>33</sup>

**Random forest.** RF is an improvement to the bagging technique, which averages the big collection of de-correlated trees.<sup>34</sup> In other words, averaging over correlated samples does not yield any new information. Therefore training samples are randomly sampled to obtain de-correlated decision trees.<sup>35</sup> It consists of numerous decision trees. Each of the trees gets independent and randomly sampled samples with the same distribution from the pool of data, and the decision made by this individual classifier is taken into account. The prediction of the RF classifier is the majority vote of the prediction of individual trees. The classification result of the new sample  $\beta$  is the prediction  $\hat{Y}_p^B$  which is shown below.

$$\hat{Y}_p^B(\beta) = \text{majority vote } \{\hat{y}_p^b(\beta)\}_1^B \quad (8)$$

Where  $b$  is the index to refer to individual trees in  $B$  number of decision trees and  $\hat{Y}_p^b$  is the prediction of tree  $b$ .

**eXtreme gradient boosting.** eXtreme gradient boosting (XGB) is a tree boosting-based algorithm proposed by Chen et al.<sup>36</sup> Boosting of decision trees works in a sequential way; in other words, underperforming trees are given more importance so that the outcome is the total response of both boosted trees and learning trees. Weight is added to the weak learners until their performance is better than a random classifier. It has an inbuilt regularization term which helps in reducing overfitting problem and parallel processing enables faster tree building and solving process. Gradient boosting classification of  $u_s$  whose prediction  $v_s$ , is given as,

$$\hat{v}_s = \sum_{n=1}^{N_{tree}} f_n(u_s) \quad (9)$$

where,  $N_{\text{tree}}$  corresponds to total number of trees and  $f_n$  are the weak learners. The objective function  $J$  can be formed as shown below,

$$\text{obj}(J) = \sum_{s=1}^S l(v_s, \hat{v}_s) + \sum_{n=1}^{N_{\text{tree}}} \Omega(f_n) \quad (10)$$

with  $l$  corresponding to loss function and  $\Omega$  is the regularization term.

**Neural network.** The simplest form of a NN is a multi-layer perceptron (MLP) and the architecture consists of hidden layers, an input layer, and an output layer. Input layer is made up of input units, output layer is made up of output units and the hidden layers contain the output units of the previous layer, and all these layers are connected by weights.<sup>37</sup> The working of a MLP can be divided into *forward pass* and *backward pass*. In the forward pass, the weighted input is passed through an activation function  $\xi$ , which propagates to the succeeding layers.

$$z_h = \xi \left( \sum_a C_{ha} \kappa_a + b_h \right) \quad (11)$$

Where,  $z_h$  is  $h^{\text{th}}$  output unit,  $\xi$  is an activation function,  $C_{ha}$  is the weight connecting  $h^{\text{th}}$  and  $a^{\text{th}}$  units,  $\kappa$  is the input, and  $b$  is the bias term. For a classification problem, the output units equal to number of classes. The final activation value ( $z$ ) is compared with the ground truth ( $z$ ) by means of a cost function,  $\mathcal{L}$ .

$$\mathcal{L}(C, b) = L(z, \hat{z}) \quad (12)$$

The error between the predicted label and the ground truth is minimized by re-calibrating the weights in the *backward pass*. The gradients of weights and bias ( $\nabla \mathcal{L}$ ) propagate backwards and the new weights are updated as a function of the gradients and the learning rate,  $\psi$ .

$$C^l = C - \psi \nabla \mathcal{L}(C, b) \quad (13)$$

This process continues until the error is reduced significantly. Detailed information about working of NNs and other NN types can be found in.<sup>38,39</sup>

### Hyperparameter space selection

In this study, a range of values is assigned to each of the hyperparameter given a classifier. The best hyperparameter space (i.e., best model) for shallow classifiers is automatically selected through grid search cross

validation (CV)<sup>40</sup> strategy with stratified group CV (Appendix B). KerasTuner, a hyperparameter optimization framework with Bayesian Optimization algorithm,<sup>41</sup> is employed to select the best hyperparameter space for MLP. Defining the range of hyperparameter values is a crucial step and it is defined based on the recommendations in the study by Pedregosa et al.<sup>40</sup> First a large range of coarse values was used to get an intuition of the range required to tune the models. The range of hyperparameter values are mentioned below.

**Support vector machines.** There are three main parameters to be chosen carefully: (1) the type of kernel function; (2)  $C$ , the regularization term which is used to penalizes the misclassifications; and (3)  $\gamma$  which mainly comes into picture when the radial basis function (RBF) or a polynomial kernel function is employed. In this study, RBF kernel is chosen given the nonlinearity of the data. The range of  $C$  is defined as:  $10^i, i \in [-1, 7]$  and  $\gamma$  is defined as:  $10^i, i \in [1, -7]$ .

**Random forest.** List of hyperparameters chosen to be tuned. (1) The number of trees: [20, 50, 100, 150, 200, 250]; (2) maximum depth a tree: [2, 6, 10, 15, 20]; (3) minimum number of samples to be present in a node for further splitting: [2, 5, 10, 15, 20]; and (4) maximum number of samples to draw from training data set to train the base estimator: [50, 100, 200, 300, 400].

**eXtreme gradient boosting.** In XGB there are four categories of parameters, namely: General parameters, Booster parameters, Learning task parameters, and Command line parameters. The tunable parameters are (1) The number of trees: [20, 50, 150, 250, 350]; (2) maximum depth of a tree: [2, 5, 10, 15, 20]; (3) learning rate: [0.001, 0.05, 0.01, 0.3, 0.5]; and (4) column sampling: [0.05, 0.1, 0.3, 0.5, 0.7].

**Multi-layer perceptron.** Some of the parameters used for tuning: (1) Adam optimizer with learning rate sampled from  $[1e-4, 1e-2]$  with logarithmic sampling method; (2) hidden layers: [1, 2, 3]; and (3) hidden units: [5, 20] with steps = 3.

### Performance evaluation and reliability assessment

The performance of ML models is evaluated using performance measures; their selection depends on the main objective of the evaluation. They can broadly be

categorized into three groups as listed in the study by Ferri et al.<sup>42</sup>

- *Threshold-based measures:* These measures are used when the total prediction error is to be minimized. Examples include accuracy, *F*-score, Kappa statistic, and so on. Some of the measures are suitable for balanced and/or imbalanced data sets.
- *Probabilistic measures:* These measures quantify the uncertainty in the predictions and are useful to assess the reliability of a classifier. Some examples include cross-entropy and Brier score.
- *Rank-based measures:* They do not focus on minimizing prediction errors based on the quality of one particular choice of threshold; rather, they measure the class separability of a classifier at different thresholds. Receiver operating characteristic (ROC) curve, precision-recall (PR) curve, and area under these curves fall in this category.

In the SHM domain, the damaged case is labeled as a positive instance and the undamaged case as a negative instance. The false positives (damage indication when it is not present) incur downtime, which causes revenue loss and results in a less reliable SHM system. Whereas, for misclassifications, false negatives (no damage indication even though it is present) means the risk of human life (in the case of rail and aircraft applications) is at stake. Furthermore, it is desirable to have trade-offs between false positives and false negatives, that is, when an SHM application is focused more on costs than life-safety, false positives need to be minimized (false positive is given more emphasis than false negative). On the other hand, if life safety is of paramount importance, then false negatives need to be minimized (false negative is given more emphasis than false positive).<sup>43</sup> Especially in aircraft applications, a trade-off between false positives and false negatives is desired. Therefore, a performance measure providing this trade-off becomes essential.

One more commonly encountered problem in a SHM system is that, undamaged instances usually outnumber damaged ones because the continuous acquisition of sensor data comes from a healthy condition and damage episode seldom occurs. Consequently, there is a natural imbalance in the data, and in such scenarios, not all measures are effective. In such cases, measures, which are less sensitive to class skew are appropriate. Rank-based measures are not sensitive to class skew, whereas threshold-based measures are sensitive to class skew. Hence, the ability of a classifier to separate a positive class from a negative class does not suffer while using rank-based measures.<sup>44</sup>

The trade-off between false positives and false negatives can be obtained by plotting a ROC curve. It is a

graphical representation of false positive rate versus true positive rate; each point on the ROC curve corresponds to a unique threshold. It gives an excellent visual of the behavior of a classifier on a given dataset, and a trade-off between false positives and false negatives. A single quantity of measure derived from the ROC curve is area under the curve (AUC), which is used in addition to provide more clarity.<sup>45</sup> The PR curve is one more measure that does not provide very optimistic results like ROC in the case of data imbalance because it focuses more on the minority class.<sup>46</sup> In this study, the AUC of ROC curves is used to measure the performance of classifiers on balanced data and the AUC of PR curves for imbalanced data; from here on we refer to them as ROC\_AUC and PR\_AUC respectively.

The probability of detection assesses the reliability of a monitoring system which is widely being used in the NDT community. It's a fundamental evaluation technique that informs as to what size of defect the system can detect with 95% confidence. Usually, the critical defect size is supposed to be less than  $a_{90|95}$  value to qualify a monitoring system as a reliable one.<sup>47</sup> The probability of detection is determined using two methods; one of them is the hit-miss method which is based on binary data and signal response analysis.<sup>48</sup> In this study, since we use ML algorithms for classification, the prediction results are binary data. This type of data is appropriate to compute the probability of detection curve using the hit-miss method. The probability of detection (POD) analysis of the ML predictions helps analyze the detectability of the defect sizes, thereby assesses the reliability of a ML-based damaged detection.

## Experimental validation

### *Parametric study to select AR features*

As shown in Figure 7, 40 AR parameters are extracted from pristine and damage signals. From here on, AR parameters and features are used interchangeably. To determine how many of those 40 parameters are necessary to obtain the best performance, a parametric study is conducted by varying the AR parameters and training samples. Note that the parametric study's primary focus is selecting the optimal number of features, not the number of training samples. The left side flowchart as shown in Figure 8 presents the parametric study methodology, wherein the first stage forms groups of aggregated baselines and damage signals, then features are extracted through AR modeling of group 1 and group 2 signals.

A feature set containing six varying features starting from four with step six in increasing order is formed. Similarly, a training sample set is formed with five

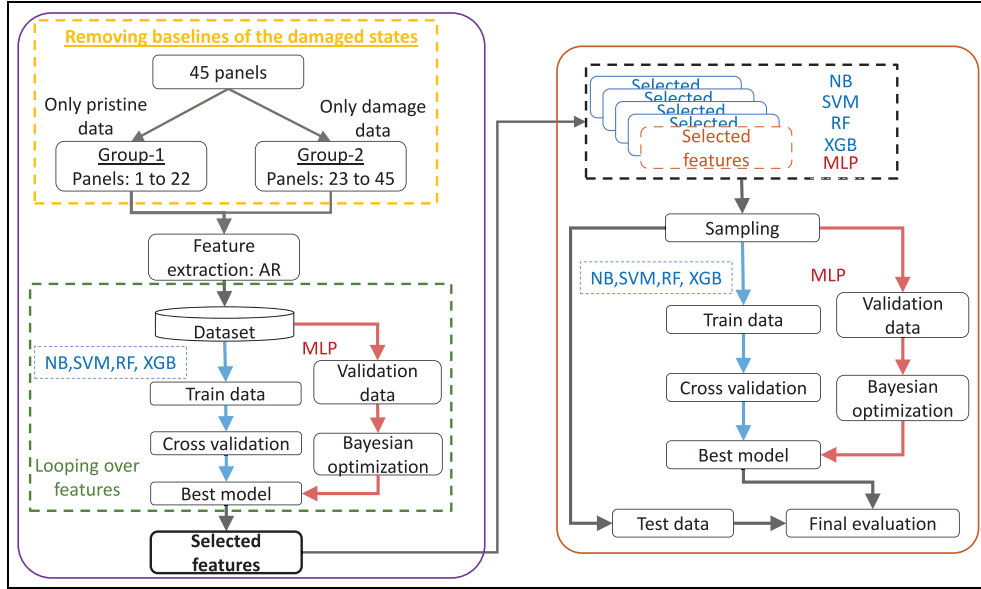


**Figure 8.** The left side flowchart shows the feature selection schema starting from feature extraction applied on grouped classes, followed by hyperparameter space optimization algorithms to determine the required features. The right-side flowchart shows the final training and evaluation procedures, starting from considering selected features from the feature selection schema. The best shallow and MLP models are obtained by grid search CV and KerasTuner with Bayesian Optimization algorithm, respectively. MLP: multi-layer perceptron; CV: cross validation.

varying training sample sizes. These two formed sets result in a total of 30 combinations of features and training sample sizes. For each of the 30 combinations, the best hyperparameter space (i.e., best model) for shallow classifiers is automatically selected through grid search CV with stratified group CV (the CV groups formed are equivalent to the number of CFRP panels to enable the models to train on signals from some panels and validate on an entirely different set of panels) and for MLP KerasTuner with Bayesian Optimization algorithm is employed. For each of the 30 combinations and for each of the classifiers, the mean of the CV scores based on ROC\_AUC is plotted as shown in Figure 9. The X-axis shows the increasing volume of training samples, Y-axis shows the increasing number of features, and the Z-axis presents the validation results (i.e., ROC\_AUC score).

All the plots correspond to each of the classifiers in Figure 9 exhibit increasing ROC\_AUC scores with the increasing number of features and training samples. This increment can be tracked by the elevation of the plots and dark red color shades, which correspond to higher ROC\_AUC. The minimum number of required features is selected based on the best-performing model given the combination of features and training samples. All classifiers' best models are obtained at 16 features, and the cross marker (×) indicates this selection

on the plots. Therefore, for the final training and evaluation of the classifiers, the selected 16 features are used.

### Model training and evaluation with uncertainty assessment

The final training set used for training the five classifiers can be represented as  $T = (X_1, X_2, \dots, X_{N_{\text{train}}})$ .  $T \in \mathbb{R}^{N_{\text{train}} \times \eta}$ , where  $N_{\text{train}} = 866$  (train samples) and  $\eta = 16$  features selected from feature-selection study for the balanced case. The entire training methodology is presented in the right flowchart in Figure 8. In the first stage of the process, selected features (resulting from the feature selection schema) corresponding to each of the classifiers is used. In the second step, pristine samples are randomly sampled to construct balanced data sets, for path identification process (see Figure 10) results in fewer damage samples in group 2 than pristine samples in group 1. Depending on the type of classifier used either grid search CV or Bayesian optimization techniques are employed to find out the best hyperparameter space on the train set suitable to learn to distinguish pristine and damage features. The CV is performed according to the stratified group CV strategy, wherein signals acquired on each panel are treated as an individual group. Herewith, this CV

strategy allows the classifiers to build the best models by training on features corresponding to some panels and predicting classes from unexposed panels. The trained best models predict the classes in the unseen test set in the evaluation stage. The small volume of the data set introduces variability in the sampling stage (when pristine samples are drawn to form a balanced data set) and in the formulation of train-validation-test sets stage. Therefore, to evaluate the skill of a classifier, sampling with replacement technique is employed, whereby pristine samples are drawn randomly with replacement five times in the sampling stage and train-validation-test sets are formed by randomly drawing pristine and damage samples five times (see Figure 8). The random drawing of samples with replacement in both the stages results in a total of 25 times random sampling. This procedure ensures that, both good and bad performing models are evaluated and the mean of the results gives an accurate and robust estimate of a classifier's skill when evaluated on unseen test data. The best selected hyperparameters of each of the classifiers corresponding to the first model among 25 models is presented in Appendix A, Table A1. The accurate estimates of all the classifiers in the form of mean ROC curves and mean AUC scores along with the variance is presented in Figure 11. The ROC curve represents the false positive rate along the  $X$ -axis and the true positive rate along  $Y$ -axis. The diagonal line represents a model with no skill, that is, which cannot discriminate between two classes and predicts a constant class for all thresholds. Furthermore, if the curve is above this line, the classifier learns helpful information (called a skillful model). In contrast, if the curve is below the line, the classifier is not learning anything.

A classifier is said to have the best performance when the point in the ROC curve is bowing toward the top left corner. Comparing performances of multiple classifiers based on the ROC curve is cumbersome. Therefore, a single scalar measure, AUC, is often used as a performance metric. In Figure 11, the AUCs are shown with corresponding deviation due to 25 models. All the classifiers registered more than 90% AUC on test data, meaning that the classifiers are learning to distinguish between pristine and defect classes. NB, used as a reference classifier, yielded the lowest mean AUC of 91%. In comparison, the other classifiers exhibited 94 and 95% AUC. The results suggest that, given the complexity of the data set, the classifiers can better separate defect and pristine classes. Table 3 shows the mean train scores and test scores.

As discussed in performance evaluation section, the SHM system often results in imbalanced pristine and defect instances. Therefore, a thorough study is

conducted to test how close the classifiers' performance with imbalance gets to that with the balanced case. To this end five imbalanced data sets are prepared (artificially) with varying imbalance ratios (IRs), namely 60–40%, 80–20%, 90–10%, and 95–5% (pristine–damage%). However, train samples and test samples are kept constant for all data sets and is same as for the balanced data set, that is, 886 train samples and 278 test samples. The same methodology is applied for all the considered imbalance cases as shown in Figure 8. However, in the sampling stage, both pristine and damage samples are randomly sampled with replacement. The mean of the CV score, that is, PR\_AUC is presented in Figure 12 with error bars representing the variance. The best set of hyperparameters corresponding to the first among the 25 models are presented in Appendix A, Table A1. The plot contains the mean test scores of all the classifiers. The PR\_AUC is along the  $Y$ -axis and the ratio of pristine samples is along the  $X$ -axis. Some of the observations are listed below,

- With increasing IR:
  - The mean scores of all the classifiers decrease gradually.
  - The variance of the test scores increased, but the variance of RF and XGB is lower compared to others.
- The best performance is observed when the data set is balanced and is worst for strong IR.
- At 60% IR and 50% pristine ratio, no significant change in the performance is observed. But for further reduction in the minority class ratio, the performance starts decreasing significantly.
- NB exhibited the lowest mean score for balanced case and the rest of the classifiers showed higher mean scores.

Creating imbalances reduces representative samples of the minority class, which makes it difficult for the classification algorithms to learn to distinguish from the majority class. The experimental data used here needs to be larger; therefore, creating an imbalance further reduces the representative samples from an already small-sized data set. Hence, degradation in the classifiers' performance is observed with increasing imbalance.

### *POD analysis*

Following the classification of GW signals, the next step involves analyzing the classification results using probability of detection to identify what defect sizes are being correctly detected. The data set contains signals corresponding to 4 frequencies and the defect size

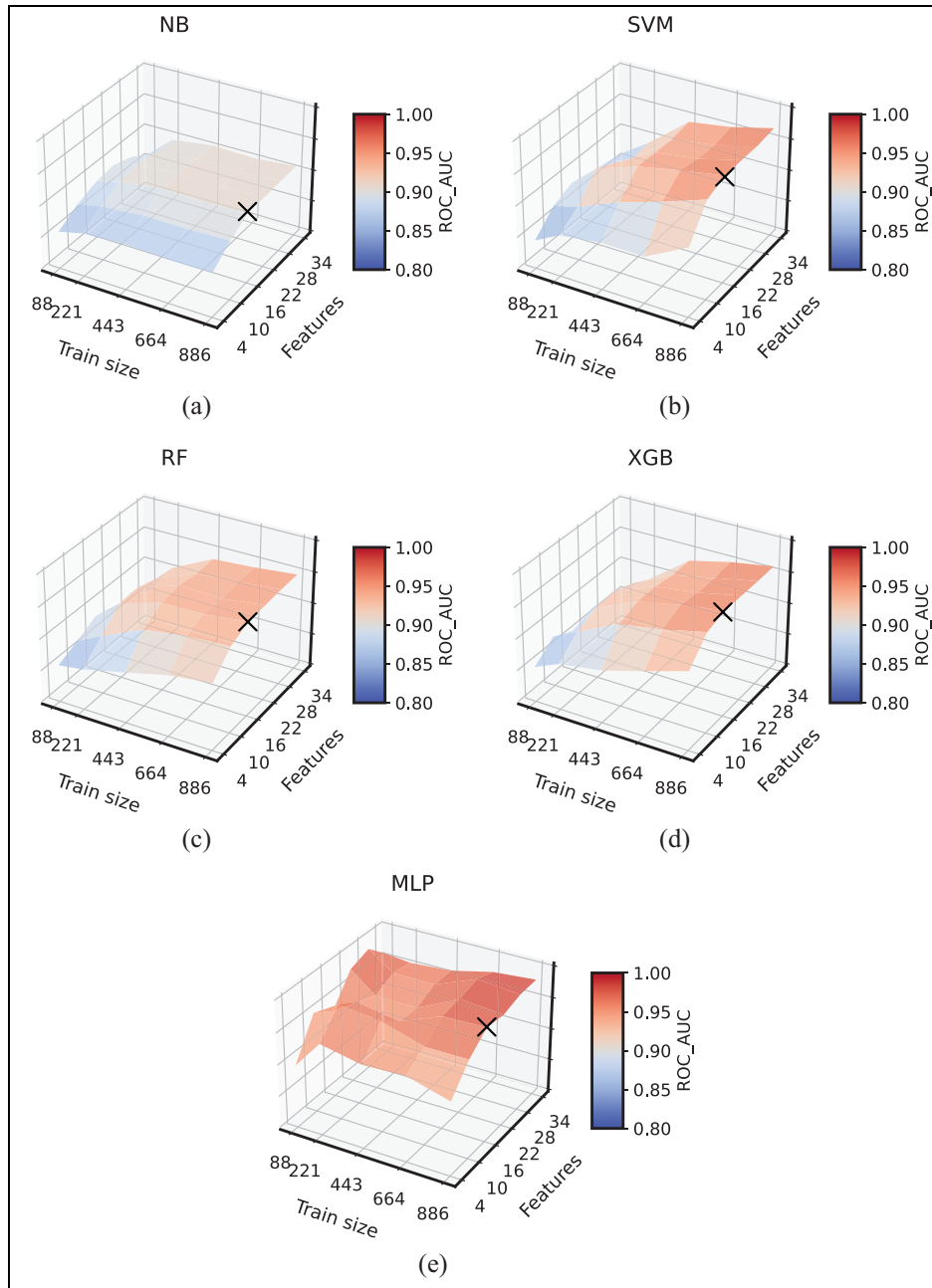


**Figure 9.** Surface plots representing the learning of classifiers as a function of features and training samples of (a) Naive Bayes, (b) support vector classifier, (c) RF, (d) XGB, and (e) MLP. The X-axis shows size of the train set, Y-axis shows number of features, and Z-axis shows the mean ROC\_AUC score. The cross markers (×) on each of the plots indicate the selection of necessary features resulting in best performing models; the necessary features selected are 16. NB: Naive Bayes; RF: random forest; XGB: eXtreme gradient boosting; MLP: multi-layer perceptron; ROC: receiver operating characteristic; AUC: area under the curve; SVM: support vector machines.

varies from 14 to 27.5 mm. Hit/Miss algorithm is employed on the predicted defect classes to compute the probability of detection curve. Since the trend in the plots obtained from all the classifiers' predictions is similar, just one plot obtained from SVM is presented

in Figure 13. Along the X-axis are the defect sizes and % probability of detection along Y-axis. The trend observed in the plot suggests that, larger defects are identified accurately which is a good indication for the damage detection system.



**Table 3.** The mean train and test ROC\_AUC scores and the variance of the predicted results for the balanced data set.

Classifiers	Train score (ROC_AUC)	Test score (ROC_AUC)
NB	0.9128 ± 0.01	0.91 ± 0.02
SVM	0.958 ± 0.03	0.94 ± 0.03
RF	0.975 ± 0.02	0.94 ± 0.02
XGB	0.99 ± 0.01	<b>0.95 ± 0.01</b>
MLP	0.98 ± 0.007	<b>0.95 ± 0.01</b>

ROC: receiver operating characteristic; AUC: area under the curve; NB: Naive Bayes; SVM: support vector machines; RF: random forest; XGB: eXtreme gradient boosting; MLP: multi-layer perceptron.  
Highest scores are highlighted with bold fonts.

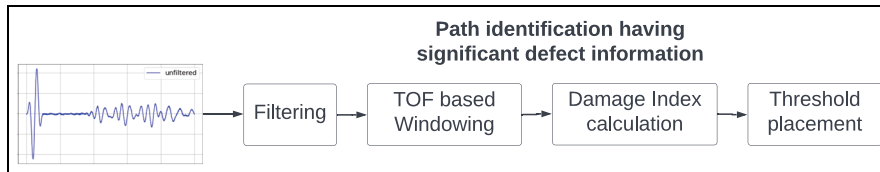


**Figure 10.** Process used for performing data annotation.

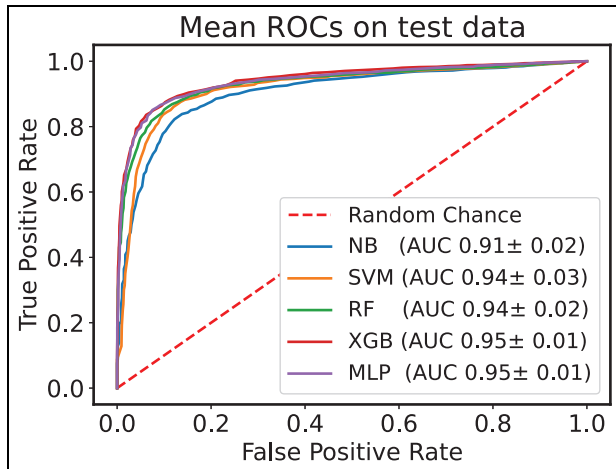


**Figure 11.** Mean ROC curves and AUC with standard deviation computed on balanced test data set.  
ROC: receiver operating characteristic; AUC: area under the curve.

## Discussion

In the previous sections, we showed the challenges in damage detection due to intra- and inter-specimen variability by considering the measurements acquired on 45 CFRP panels. We performed the analysis by considering variability inclusion and baseline aggregation. Furthermore, an AR-based feature extraction method is applied to avoid using baseline correction methods, and classifiers are used for the detection task. The

results obtained show an excellent classification performance of 95% (ROC\_AUC) and show the robustness of the approach to intra- and inter-specimen viability. The data set presented in the previous section contains a minor variation in the temperature. Therefore, an alternative data set is considered to investigate the effect of the temperature (i.e., OpenGW<sup>22</sup>), and the same methodology is applied to it.

## Impact of temperature variation: a preliminary study

The GW signals measured on CFRP panels with real-impact-caused delaminations were analyzed in the previous data set. Unfortunately, the experiment campaign was carried out in a laboratory setup with minor temperature variations. On the other hand, it is well known that temperature variation can significantly influence GW propagation in both isotropic and anisotropic materials. Therefore, to provide a preliminary validation of our proposed methodology in the presence of high-temperature variation, we decided to consider the OpenGW<sup>22</sup> data set, which contains measurements performed on CFRP with temperature variation between 20 and 60°C. It is also worth mentioning that the instrumentation and artificial defect (mass attachment) makes this problem more academic than the previous one (brief details about the OpenGW data set are given below). Nevertheless, we believe the proposed methodology can directly be applied to this data set to assess

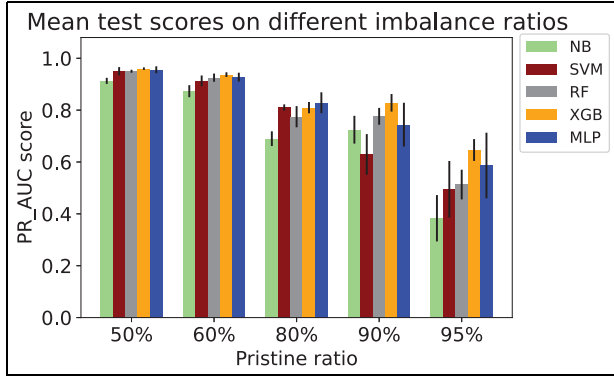


**Figure 12.** Mean test precision-recall AUC with variance depicted in error bars for all the IR and classifiers resulting from 25 models. AUC: area under the curve; IR: imbalance ratio.

the robustness of baseline aggregation and AR-based feature extraction under significant temperature variations.

The measurements are conducted on a composite plate instrumented with 12 piezoelectric transducers, and reversible damage is placed by attaching weights on different locations (see Figure 14). For a detailed explanation of the experimental setup and acquisition, the readers can refer to this article.<sup>22</sup> The study is conducted by forming four groups with increasing temperature variations, that is,  $[20^\circ\text{C}, 30^\circ\text{C}]$ ,  $[20^\circ\text{C}, 40^\circ\text{C}]$ ,  $[20^\circ\text{C}, 50^\circ\text{C}]$ , and  $[20^\circ\text{C}, 60^\circ\text{C}]$ . This particular subdivision of temperature variation enables a thorough study of the applicability of the proposed methodology on significant temperature variations. The same methodology is also applied to each temperature group, the baseline signals are aggregated so that T2, T3, T4, and T5 transducers are considered emitters. For each of these four emitters, only three paths (couples) are considered, namely, one direct path and two adjacent paths (e.g., T2→T7, T2→T8, and T2→T9). Measurement signals corresponding to damage DG12 alone are considered in this preliminary study.

The path identification schema is employed with the same threshold (i.e., 0.1) as used in the former data set to identify more defect information-carrying paths (see Figure 10). All the identified paths carrying more damage information are grouped under the damage class, and all the aggregated baselines are grouped under the pristine class. AR modeling is applied to both groups to extract the features. Five classifiers are chosen to learn to distinguish the feature space: NB, SVM, RF, XGB, and MLP. Measurements corresponding to just one excitation frequency (i.e., 40 kHz) are considered to conduct the preliminary study. However, except for

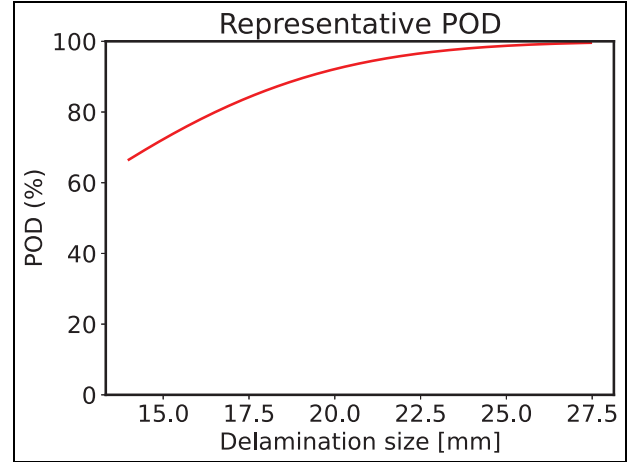


**Figure 13.** POD computed on the model predictions represented by the red curve. The POD curve shown here is the representative result of PODs obtained from all five classifiers' predictions.

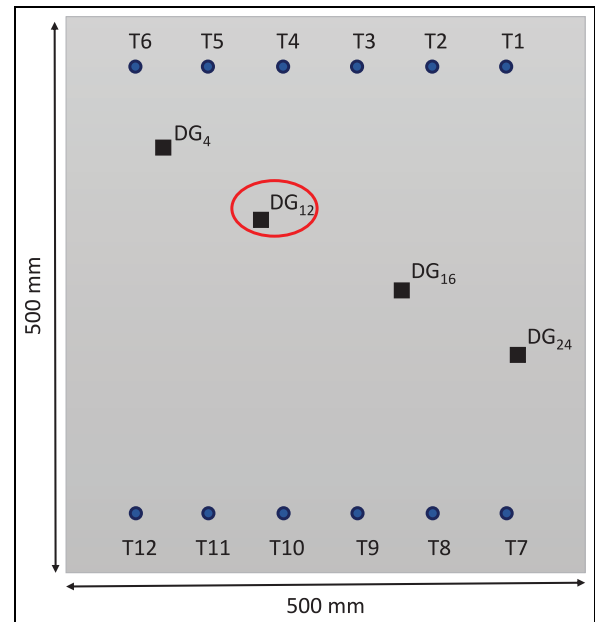


**Figure 14.** CFRP plate instrumented with 12 PZTs and a reversible damage placed at either 4 locations to acquire measurements. CFRP: carbon fiber reinforced polymer.

the CV strategy, the same feature selection and final training methodology are applied as shown in Figure 8. Features selected ( $\eta$ ) for all temperature groups are  $\eta_{\text{NB,SVM,RF,XGB}} = 5$  and  $\eta_{\text{MLP}} = 24$ . Training samples ( $N_{\text{train}}$ ) for all temperature groups and all classifiers considered are  $N_{\text{train}} = 288, 450, 646,$  and  $1164$ .

**Table 4.** The mean train and test ROC\_AUC scores for varying temperature ranges.

Temperature variation (°C)	Train, test groups	Classifiers and ROC_AUC scores				
		NB	SVM	RF	XGB	MLP
TempGroup 1 [20, 30]	Train	0.71 ± 0.02	0.98 ± 0.006	0.97 ± 0.004	0.99 ± 4e-7	0.96 ± 0.02
	Test	0.72 ± 0.06	0.87 ± 0.04	0.86 ± 0.01	<b>0.89 ± 0.04</b>	0.85 ± 0.05
TempGroup 2 [20, 40]	Train	0.723 ± 0.02	0.98 ± 0.008	0.95 ± 0.007	0.99 ± 5e-7	0.95 ± 0.02
	Test	0.726 ± 0.04	0.81 ± 0.05	0.83 ± 0.02	<b>0.88 ± 0.03</b>	0.85 ± 0.04
TempGroup 3 [20, 50]	Train	0.68 ± 0.02	0.97 ± 0.02	0.91 ± 0.004	0.99 ± 4e-7	0.89 ± 0.03
	Test	0.69 ± 0.03	0.8 ± 0.05	0.79 ± 0.01	<b>0.87 ± 0.03</b>	0.81 ± 0.02
TempGroup 4 [20, 60]	Train	0.673 ± 0.008	0.97 ± 0.003	0.85 ± 0.006	0.99 ± 4e-7	0.86 ± 0.03
	Test	0.672 ± 0.02	0.8 ± 0.02	0.76 ± 0.009	<b>0.89 ± 0.02</b>	0.77 ± 0.02

ROC: receiver operating characteristic; AUC: area under the curve; NB: Naive Bayes; SVM: support vector machines; RF: random forest; XGB: eXtreme gradient boosting; MLP: multi-layer perceptron.  
Highest scores are highlighted with bold fonts.

Furthermore, the test samples for all temperature groups and all classifiers are  $N_{\text{test}} = 92, 142, 204,$  and  $366$ . We used stratified CV<sup>40</sup> instead of group stratified CV, as only one panel is present and forming groups requires multiple panels (to perform CV similar to the previous data set). Furthermore, the hyperparameters' range is unchanged except for XGB and RF, whereby the range of some parameters are slightly adjusted. Final mean train and test ROC\_AUC scores are presented in Table 4 and the mean ROC curves for each temperature group are shown in Figure 15. From the first to the last temperature groups, NB, SVM, RF, XGB, and MLP registered a 4, 7, 10, 2, and an 8% drop, respectively, when tested on the test set. Furthermore, XGB has shown robustness and stability against small and large temperature variations with the proposed aggregated-baseline and AR-based feature extraction approach.

### Comparison to the state-of-the-art and discussion

These results obtained can be considered promising when compared with very recent works on the same data set<sup>20,23</sup> mentioned in the introduction. Schnur et al.<sup>20</sup> performed classification by compensating the temperature effect through optimal baseline selection and baseline signal stretch methods. Furthermore, the authors analyzed just two sensor pairs, that is, T4→T9 and T1→T7, to apply compensation methods and classification schema. With the best Fourier coefficients (features) and SVM, they showed high classification accuracy with temperature compensation. In another work, Abbassi et al.<sup>23</sup> compared four unsupervised dimensionality reduction algorithms to obtain latent vectors and used them for damage detection. They

showed high detection accuracies on four temperature groups formed between 20 and 60°C with 10°C step.

On the other hand, comparing our proposed methodology with the study by Schnur et al.<sup>20</sup> has shown to be very effective under more considerable temperature variations without the need for temperature compensation and aggregating various sensor pairs (i.e., baseline aggregation). Furthermore, comparison with the study by Abbassi et al.<sup>23</sup> shows that the proposed methodology works for shorter and wider temperature ranges, that is, [20 °C, 40 °C] and [20 °C, 60 °C], respectively.

The FPR in a GW-SHM system is generally expected to be relatively low (i.e., less than a few percent). However, depending on the application and the system, the actual FPR can vary. The results obtained with the proposed methodology suggest that the methodology is robust to substantial temperature variations. Nevertheless, the mean AUC\_ROC and, in turn, the FPR shown in Figure 15 can be further improved by enhancing the data set.

### Conclusions and perspective

In GW-SHM, intra- and inter-specimen variabilities have significant impact on the reliability of detection systems. A methodology is proposed containing variability inclusion and baseline aggregation. With AR-based features and classifiers, the final classification results show that classifiers can distinguish the two classes and have the highest classification performance of 95% ROC\_AUC by XGB and MLP. The results suggest that the methodology is robust to variabilities such as instrumentation, material properties, damage size, and location.

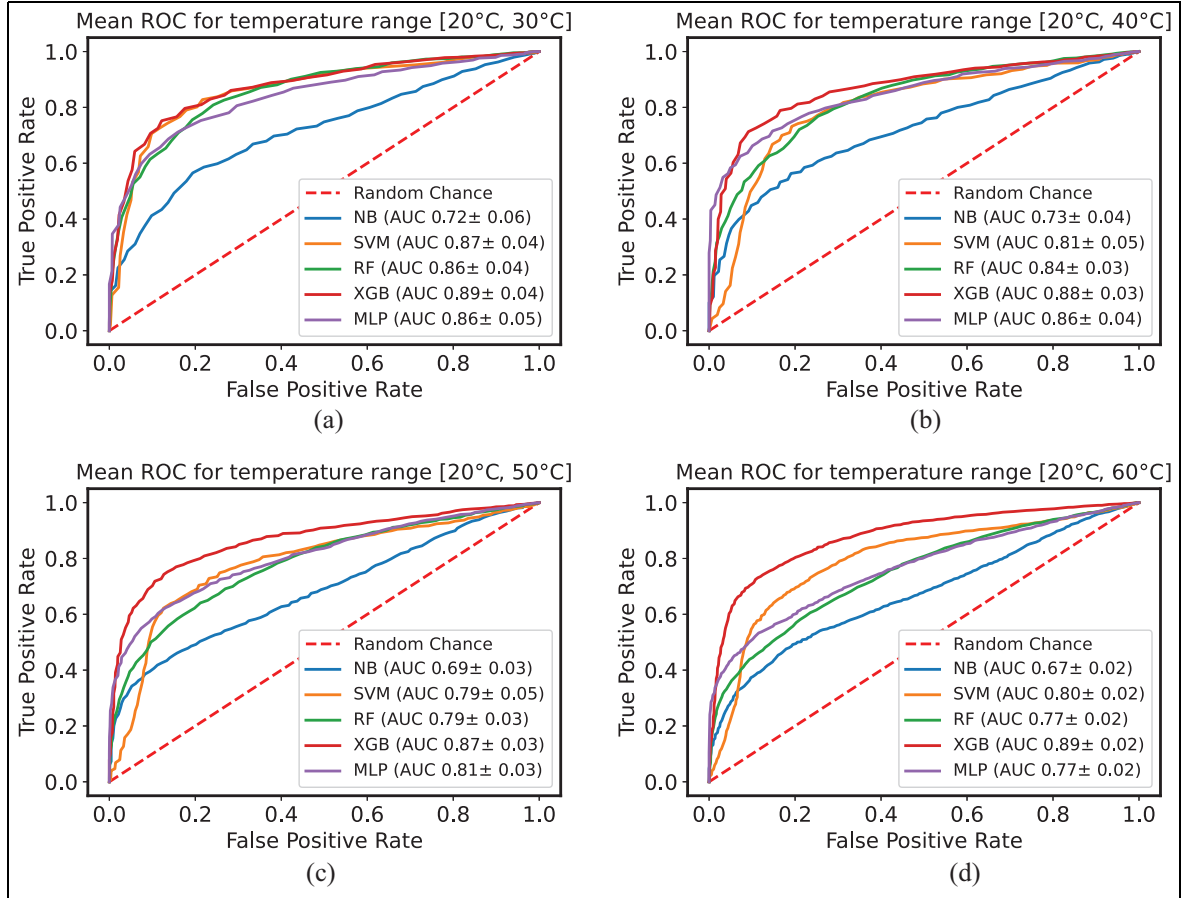


**Figure 15.** Mean ROC curves with AUC values computed on the test set for temperature variations (a) [20°C, 30°C], (b) [20°C, 40°C], (c) [20°C, 50°C], and (d) [20°C, 60°C]. ROC: receiver operating characteristic; AUC: area under the curve.

To study the impact of significant temperature variations (absent in the former data set), we consider an alternative data set based on GW measurements on CFRP (i.e., OpenGW data set). The same proposed methodology is applied to this data set. For increasing temperature variations, an average of 5% drop in the performance of the classifiers is observed, except for XGB, which registered only a 2% drop; furthermore, for all the temperature variations, XGB exhibited an average of 89% ROC\_AUC, suggesting that it is the more robust and stable classifier to large temperature variations. Furthermore, XGB classifier has shown to be the most robust classifier on both the data sets (i.e., inter-specimen variability and large temperature variations).

Our future research will focus on the performance of the robustness of classification algorithms based on

GW signals under the influence of intra- and inter-specimen and temperature variability. Toward this end, simulations can add synthetic data to the measurements as a data augmentation procedure based on physics.

### Acknowledgement

The authors would like to thank Dr Arnaud Recoquillay for providing valuable suggestions and advices particularly during the revision phase.

### Author contributions

VN was involved in conceptualization, formal analysis, methodology, software, wrote—original draft, wrote—review and editing. OM was involved in conceptualization and supervision. RM was involved in conceptualization, supervision, methodology and wrote—review and editing. OD was

involved in project administration, funding acquisition, and resources.



### Declaration of conflicting interests

The author(s) declared no potential conflicts of interest with respect to the research, authorship, and/or publication of this article.

### Funding

The author(s) disclosed receipt of the following financial support for the research, authorship, and/or publication of this article: This work was supported by the European Union's Horizon 2020 research and innovation program under the Marie Skłodowska-Curie grant agreement [grant number: 860104].

### ORCID iDs

Vivek Nerlikar  <https://orcid.org/0000-0003-2115-7931>  
Roberto Miorelli  <https://orcid.org/0000-0003-3728-2227>

### References

1. Farrar CR, Czarnecki JJ, Sohn H, et al. A review of structural health monitoring literature 1996-2001. Technical Report LA-13976-MS, Los Alamos National Laboratory, Los Alamos, New Mexico, USA, 2003.
2. Mitra M and Gopalakrishnan S. Guided wave based structural health monitoring: a review. *Smart Mater Struct* 2016; 25(5): 053001.
3. Xu B and Giurgiutiu V. Single mode tuning effects on lamb wave time reversal with piezoelectric wafer active sensors for structural health monitoring. *J Nondestr Eval* 2007; 26(2-4): 123-134.
4. Gorgin R, Luo Y and Wu Z. Environmental and operational conditions effects on lamb wave based structural health monitoring systems: a review. *Ultrasonics* 2020; 105: 106114.
5. Lu Y and Michaels JE. A methodology for structural health monitoring with diffuse ultrasonic waves in the presence of temperature variations. *Ultrasonics* 2005; 43(9): 717-731.
6. Croxford AJ, Wilcox PD, Konstantinidis G, et al. Strategies for overcoming the effect of temperature on guided wave structural health monitoring. In: Kundu T (ed.) *Health monitoring of structural and biological systems 2007*, vol. 6532, pp. 590-599. Bellingham, Washington: International Society for Optics and Photonics, SPIE, 2007.
7. Croxford AJ, Moll J, Wilcox PD, et al. Efficient temperature compensation strategies for guided wave structural health monitoring. *Ultrasonics* 2010; 50(4-5): 517-528.
8. Douglass ACS and Harley JB. Dynamic time warping temperature compensation for guided wave structural health monitoring. *IEEE Trans Ultrason Ferroelectr Freq Control* 2018; 65(5): 851-861.
9. Fendzi C, Rébillat M, Mechbal N, et al. A data-driven temperature compensation approach for structural health monitoring using lamb waves. *Struct Health Monit* 2016; 15(5): 525-540.
10. Mariani S, Heinlein S and Cawley P. Location specific temperature compensation of guided wave signals in structural health monitoring. *IEEE Trans Ultrason Ferroelectr Freq Control* 2020; 67(1): 146-157.
11. Mariani S, Heinlein S and Cawley P. Compensation for temperature-dependent phase and velocity of guided wave signals in baseline subtraction for structural health monitoring. *Struct Health Monit* 2019; 19(1): 26-47.
12. Mariani S and Cawley P. Change detection using the generalized likelihood ratio method to improve the sensitivity of guided wave structural health monitoring systems. *Struct Health Monit* 2020; 20(6): 3201-3226.
13. Mariani S, Rendu Q, Urbani M, et al. Causal dilated convolutional neural networks for automatic inspection of ultrasonic signals in non-destructive evaluation and structural health monitoring. *Mech Syst Signal Process* 2021; 157: 107748.
14. Kulakovskiy A. *Development of a SHM system by elastic guided waves applied to aeronautic structures*. PhD Thesis, Ecole Polytechnique, 2019.
15. Ing RK and Fink M. Self-focusing and time recompression of lamb waves using a time reversal mirror. *Ultrasonics* 1998; 36(1-5): 179-186.
16. Park S, Lee C and Sohn H. Reference-free crack detection using transfer impedances. *J Sound Vib* 2010; 329(12): 2337-2348.
17. Alem B, Abedian A and Nasrollahi-Nasab K. Reference-free damage identification in plate-like structures using lamb-wave propagation with embedded piezoelectric sensors. *J Aerosp Eng* 2016; 29(6): 04016062.
18. Miorelli R, Kulakovskiy A, Chapuis B, et al. Supervised learning strategy for classification and regression tasks applied to aeronautical structural health monitoring problems. *Ultrasonics* 2021; 113: 106372.
19. Bai L, Le Bourdais F, Miorelli R, et al. Ultrasonic defect characterization using the scattering matrix: A performance comparison study of Bayesian inversion and machine learning schemas. *IEEE Trans Ultrason Ferroelectr Freq Control* 2021; 68(10): 3143-3155.
20. Schnur C, Goodarzi P, Lugovtsova Y, et al. Towards interpretable machine learning for automated damage detection based on ultrasonic guided waves. *Sensors* 2022; 22(1): 406.
21. Rautela M, Senthilnath J, Moll J, et al. Combined two-level damage identification strategy using ultrasonic guided waves and physical knowledge assisted machine learning. *Ultrasonics* 2021; 115: 106451.
22. Moll J, Kexel C, Pöttsch S, et al. Herrmann. Temperature affected guided wave propagation in a composite plate complementing the open guided waves platform. *Sci Data* 2019; 6(1): 191.
23. Abbassi A, Römgens N, Tritschel FF, et al. Evaluation of machine learning techniques for structural health monitoring using ultrasonic guided waves under varying temperature conditions. *Struct Health Monit* 2022; 22: 147592172211075.

24. Nagaz K. *Sources of variability linked to manufacturing parameters of structural features of aeronautical composite structures*. Theses, Université Paul Sabatier–Toulouse III, July 2022.
25. Jennings CL, Montgomery D and Kulahci M. *Introduction to time series analysis and forecasting*. Wiley series in probability and statistics, 2nd edn. Hoboken, NJ: Wiley, 2015.
26. Nardi D, Lampani L, Pasquali M, et al. Detection of low-velocity impact-induced delaminations in composite laminates using auto-regressive models. *Compos Struct* 2016; 151: 108–113.
27. Figueiredo E, Figueiras J, Park G, et al. Influence of the autoregressive model order on damage detection. *Comput Aided Civ Infrastruct Eng* 2010; 26(3): 225–238.
28. Dao PB and Staszewski WJ. Cointegration approach for temperature effect compensation in lamb-wave-based damage detection. *Smart Mater Struct* 2013; 22(9): 095002.
29. Zhou Q, Ning Y, Zhou Q, et al. Structural damage detection method based on random forests and data fusion. *Struct Health Monit* 2012; 12(1): 48–58.
30. Dong W, Huang Y, Lehane B, et al. XGBoost algorithm-based prediction of concrete electrical resistivity for structural health monitoring. *Autom Constr* 2020; 114: 103155.
31. Zhang H. The optimality of naïve bayes. In: *In FLAIRS2004 conference*, Washington DC, USA: AAAI Press, 2004.
32. Boser BE, Guyon IM and Vapnik VN. A training algorithm for optimal margin classifiers. In: *Proceedings of the fifth annual workshop on computational learning theory–COLT '92*. ACM Press, 1992.
33. Kecman V. Support vector machines – an introduction. In: Wang L (ed.). *Support vector machines: theory and applications*. Berlin, Germany; Heidelberg, Germany: Springer, 2005, pp. 1–47.
34. Breiman L. Random forests. *Mach Learn* 2001; 45(1): 5–32.
35. Nordhausen K. The elements of statistical learning: data mining, inference, and prediction, second edition by Trevor Hastie, Robert Tibshirani, Jerome Friedman. *Int Stat Rev* 2009; 77(3): 482–482.
36. Chen T and Guestrin C. *Xgboost: a scalable tree boosting system*. New York, USA: ACM; 2016.
37. Shin HC, Orton M, Collins DJ, et al. Organ detection using deep learning. In: *Medical image recognition, segmentation and parsing*. Amsterdam, Netherlands: Elsevier, 2016, pp. 123–153.
38. Chollet F. *Deep learning with python*. Shelter Island, New York: Manning Publications, 2017.
39. Heaton J, Goodfellow I, Bengio Y, et al. Deep learning. *Genet Program Evolvable Mach* 2017; 19(1–2): 305–307.
40. Pedregosa F, Varoquaux G, Gramfort A, et al. Scikit-learn: machine learning in python. *J Mach Learn Res* 2011; 12: 2825–2830.
41. O'Malley T, Bursztein E, Long J, et al. Kerastuner. Available at: <https://github.com/keras-team/keras-tuner> (2019, accessed November 2022).
42. Ferri C, Hernández-Orallo J and Modrou R. An experimental comparison of performance measures for classification. *Pattern Recognit Lett* 2009; 30(1): 27–38.
43. Figueiredo E and Santos A. Machine learning algorithms for damage detection. In: Nobari AS and Aliabadi MHF (eds.), *Vibration-based techniques for damage detection and localization in engineering structures*. Singapore: World Scientific (Europe), 2018, pp. 1–39.
44. Ma H. *Imbalanced learning*. Hoboken, NJ: John Wiley Sons, 2013.
45. Bradley AP. The use of the area under the ROC curve in the evaluation of machine learning algorithms. *Pattern Recognit* 1997; 30(7): 1145–1159.
46. Saito T and Rehmsmeier M. The precision-recall plot is more informative than the ROC plot when evaluating binary classifiers on imbalanced datasets. *PLOS One* 2015; 10(3): e0118432.
47. Tschoke K, Mueller I, Memmolo V, et al. Feasibility of model-assisted probability of detection principles for structural health monitoring systems based on guided waves for fiber-reinforced composites. *IEEE Trans Ultrason Ferroelectr Freq Control* 2021; 68(10): 3156–3173.
48. Monaco E, Memmolo V, Ricci F, et al. Guided waves based SHM systems for composites structural elements: statistical analyses finalized at probability of detection definition and assessment. In: Kundu T (ed.). *Proc. SPIE 9438, Health Monitoring of Structural and Biological Systems*, San Diego, CA: SPIE, 2015.

## Appendix A

### Best selected hyperparameter combination

## Appendix B

### Cross validation for machine learning model selection

Except for Naive Bayes, the rest of the classifiers contain hyperparameters, and their selection defines the model suitable for the data present at hand. Furthermore, an appropriate selection of hyperparameters counter overfitting and/or underfitting problems. Hyperparameter selection is carried out through cross validation (CV). In this work, the data is coming from multiple panels; therefore, group CV strategy is



**Table A1.** Shows the list of best hyperparameters and features selected of the first model among 25 models.

Classifier	Hyperparameter and features	IR Pristine ratio (%)				
		50	60	80	90	95
SVM	AR features ( $\eta$ )	16	14	16	28	16
	C	0.1	1	100	1e3	1
	gamma	0.1	0.1	1e-3	1e-5	0.001
RF	AR features ( $\eta$ )	16	20	8	28	10
	max_depth	15	10	10	15	10
	max_samples	400	400	200	100	400
	min_samp_split	10	2	10	5	15
	n_estimators	100	250	50	100	100
XGB	AR features ( $\eta$ )	16	12	8	28	22
	colsample_bynode	0.05	0.3	0.05	0.5	0.1
	learning_rate	0.01	0.05	0.01	0.5	0.05
	max_depth	2	6	10	10	15
	n_estimators	150	250	50	50	100
MLP	AR features ( $\eta$ )	16	28	14	14	18
	hidden_layer	3	1	1	3	2
	hidden_units	(20,11,5)	20	20	(20,20,5)	(20,20)
	learning_rate	0.01	0.01	0.01	0.00056	0.01

AR: AutoRegression; SVM: support vector machines; RF: random forest; XGB: eXtreme gradient boosting; MLP: multi-layer perceptron; IR: imbalance ratio.

suitable, and this strategy enables to check how well the models generalize on unseen groups of panels.<sup>40</sup> The stratified group CV method ensures equal distribution of class labels in the train and validation set at each fold. The working principle behind group CV is that the training set is grouped according to the number of panels and is divided into  $k$  folds where  $k$  is the number of splits. In other words, the training set is divided into  $k$  subsets of groups. Out of  $k$  subsets,

$(k - 1)$  subsets only are used for training on a given set of hyperparameters, and the model is validated on the remaining subset of groups. It is an iterating scheme, which means that in the next iteration, the left-out subset becomes a part of the training sample, and a different subset of groups is held out for validation. This iteration repeats  $k$  times, and the final performance measure is the average performance measure on the validation sets at each iteration.